Level structure in the transitional nucleus ^{215}Fr

Khamosh Yadav,[1] A. Y. Deo,[1,*] Madhu,[1] Pragati,[1] P. C. Srivastava,[1] S. K. Tandel,[2] S. G. Wahid,[2] S. Kumar,[3] S. Muralithar,[4] R. P. Singh,[4] Indu Bala,[4] S. S. Bhattacharjee,[4,†] Ritika Garg,[4] S. Chakraborty,[5] S. Rai,[6] and A. K. Jain[1,7]

[1]*Department of Physics, Indian Institute of Technology Roorkee, Roorkee 247667, India*
[2]*School of Physical Sciences, UM-DAE Centre for Excellence in Basic Sciences, University of Mumbai, Mumbai 400098, India*
[3]*Department of Physics and Astrophysics, University of Delhi, New Delhi 110007, India*
[4]*Inter-University Accelerator Centre, Aruna Asaf Ali Marg, New Delhi 110067, India*
[5]*Variable Energy Cyclotron Centre, Kolkata 700064, India*
[6]*State Forensic Science Laboratory, 37/1/2 Belgachia Road, Kolkata 700037, India*
[7]*Amity Institute of Nuclear Science and Technology, Amity University, Noida 201303, India*

(Received 1 November 2021; accepted 18 February 2022; published 3 March 2022)

The level scheme of ^{215}Fr is extended up to $55/2\ \hbar$ and 4.8 MeV excitation energy with the addition of 52 new γ-ray transitions. Previously established isomers and their half-lives, except for the $47/2^+$ state, are revisited. The discrepancy in the half-life of the $39/2^-$ state is resolved, and its half-life is revised to 11.4(14) ns. An overall good agreement is observed between the experimental results and the shell-model calculations performed using the CD-Bonn NN interaction derived from the $V_{\text{low-}k}$ renormalization approach. A weak coupling of the odd proton to the even-even core is observed to account for the level structure at lower energies, which strongly resembles a decoupled nonrotational band. A new positive-parity sequence is also established which is observed to originate from the coupling of the $i_{13/2}$ proton at low excitation energy.

DOI: 10.1103/PhysRevC.105.034307

I. INTRODUCTION

Experimental nuclear structure studies in various regions of the nuclear chart aid in examining predictions of nuclear models and confining the regions of their applicability. For example, nuclei with a few valence nucleons outside the doubly magic ^{208}Pb ($Z = 82$, $N = 126$) core possess a nearly spherical shape and their spectroscopic information is interpreted well using the shell model [1–3] and more recently in the generalized seniority scheme [4], while nuclei in the actinide region ($A \approx 220$) exhibit stable "pear" shapes due to strong octupole correlations [5–9]. Several theoretical models based on the reflection-asymmetric mean-field approach [10–13], algebraic approaches [14], and α clustering [15] have been used to understand the experimental results pertaining to reflection-asymmetric nuclei [16]. Nuclear excitations in the latter region are governed by the collective degrees of freedom. The nuclei between the spherical and octupole-shape regions, known as transitional nuclei, are of considerable interest as the interplay between the two basic modes of excitations results in diverse structural phenomena. A smooth transition from the shell model to the collective regime is observed with increasing number of valence nucleons [16–18]. The onset of collectivity is reflected in the gradual enhancement of the $B(E2)$ rates and the energy systematics of the 2_1^+ and 4_1^+ states in the even-even trans-lead nuclei [17–20].

The level structures in the $N = 127$ isotones, viz., ^{213}Rn [21,22], ^{214}Fr [23,24], and ^{215}Ra [22,25,26], have been described in terms of empirical shell-model calculations. Several low- and high-spin isomers have been reported in the above studies. Similarly, a number of high-spin yrast isomers were identified in the $N = 128$ isotones, viz., ^{214}Rn [18,27] and ^{216}Ra [27,28], where the shell-model calculations accounted well for the single-particle nature of the lower-lying states. The high-spin isomers in this region are known to occur mainly due to the change in the intrinsic single-particle configurations and coupling of the single-particle states to the octupole-phonon vibrations [18,21,29]. The octupole admixed isomeric states depopulate via enhanced ($\gtrsim$22 W.u.) $E3$ transitions [30]. The origin of these transitions is mainly attributed to the availability of the high-j valence proton ($i_{13/2}$ and $f_{7/2}$) and neutron ($j_{15/2}$ and $g_{9/2}$) orbitals, which differ by $\Delta j = \Delta l = 3$ [31]. Lower $B(E3)$ rates ($\approx$3–5 W.u.) are expected for "spin-flip" transitions which correspond to an orbital change of either $\pi i_{13/2} \to \pi h_{9/2}$ or $\nu j_{15/2} \to \nu i_{11/2}$ [30,31].

The francium isotopes ($Z = 87$) with neutron number between 126 and 130 lie near the lower edge of the octupole-deformed actinide region and connect the two distinct regions of nuclear structure [16]. The level structures in the lighter francium isotopes $^{211-214}$Fr [23,32,33] display characteristic single-particle excitations, while a recent study by Pragati *et al.* reported parity-doublet structures in ^{216}Fr [34]. Although the reported level structure does not follow the regular pattern

*Corresponding author: ajay.deo@ph.iitr.ac.in
†Present address: Institute of Experimental and Applied Physics, Czech Technical University in Prague, Husova 240/5, 110 00 Prague 1, Czech Republic.

of rotational bands, enhanced octupole correlations are evident from the small energy splitting and large $B(E1)/B(E2)$ values. Thus, it was suggested that ^{216}Fr provides a lower limit ($Z = 87$ and $N = 129$) in the trans-lead region from where the octupole correlations emerge [34,35]. Therefore, a comprehensive study of ^{215}Fr is expected to yield more insights into the evolution of nuclear structure from near-spherical to octupole deformed shapes.

Prior to the present work, in-beam studies were carried out for ^{215}Fr using the ^{208}Pb(^{11}B, $4n$) and ^{204}Hg(^{15}N, $4n$) reactions [36–38]. The excited states up to $47/2\hbar$ and 3462 keV were established on the basis of the γ-γ, α-γ, and conversion-electron spectroscopy. The reported level schemes revealed that the low-lying states originate from the weak coupling of the $h_{9/2}$ proton to the even-even core. Only a few states were known from the coupling of the proton occupying the $i_{13/2}$ orbital. Several high-spin isomers with the $T_{1/2} \approx 3$–33 ns were also reported at higher excitation energies [36,37]. However, considerable disagreement between the values of the reported half-lives of the $39/2^-$ isomer was noted. In this work, we report an extended level scheme of ^{215}Fr with the addition of 52 new γ-ray transitions constituting 45 new levels. A new low-lying positive-parity sequence is observed to originate from the coupling of the $i_{13/2}$ proton to the even-even core. The half-lives of several isomeric states are confirmed and a revised value of $T_{1/2} = 11.4(14)$ ns for the $39/2^-$ state is deduced using the centroid-shift analysis.

II. EXPERIMENTAL DETAILS AND DATA ANALYSIS

Excited states in ^{215}Fr nucleus were populated using the ^{208}Pb(^{11}B, $4n$)^{215}Fr reaction. The ^{11}B beam provided from the 15 UD Pelletron accelerator at Inter-University Accelerator Centre (IUAC), New Delhi, was impinged on a ≈99% enriched self-supporting ^{208}Pb target of ≈6 mg/cm^2 thickness. The beam energy from the accelerator was allowed to vary from 54 to 62 MeV (in the laboratory frame). The Indian National Gamma Array (INGA) [39] was utilized to detect the γ rays from deexcitation of the residual nuclei. The array consisted of 14 Compton suppressed clover high-purity germanium (HPGe) detectors which were positioned at 90°, 123°, and 148° with respect to the beam direction. Two- and higher-fold coincidence data were acquired using the computer-automated measurement and control (CAMAC) based data acquisition system CANDLE [40]. The energy and (relative) efficiency calibrations of the detection system were performed using a standard ^{152}Eu source. The measured typical values of energy resolution were ≈1.5 keV at 122 keV and 2.3 keV at 1408 keV γ-ray energy. The calibrated data were written into a ROOT [41] tree format and further sorted into various two- and three-dimensional histograms. These histograms were analyzed using ROOT and RADWARE [42].

A prompt γ-γ matrix and a γ-γ-γ cube, with γ rays observed within a 100 ns coincidence window, were constructed. In addition, an asymmetric *early-delayed* matrix, with *early* axis comprising of the γ rays which proceed by 50–200 ns with respect to those on *delayed* axis, was generated to investigate isomers. The half-lives of the isomers were extracted using the centroid-shift analysis. This method is used to determine the lifetimes which are smaller compared to the full width at half maximum (FWHM) of a prompt time distribution [43]. For the present detection setup, the FWHM was observed to be around 50 ns for the transition energies around 500 keV.

For the centroid-shift analysis, a three-dimensional histogram with axes containing $E_\gamma(early)$, $E_\gamma(delayed)$ and the time difference between the two was constructed.

The multipolarities of the γ-ray transitions were extracted from the analysis based on the directional correlation from the oriented states (DCO) ratio (R_{DCO}) [44] and the linear polarization (P) measurements [45,46]. For the DCO analysis, an asymmetric γ–γ matrix was generated with one axis comprising the γ rays recorded in the detectors at 148° (θ_1) and the other at 90° (θ_2) angle. Further, the DCO ratio for the transition of interest (γ_1) is defined as

$$R_{\mathrm{DCO}} = \frac{I_{\gamma_1} \text{ at } \theta_1 \text{ gated by } \gamma_2 \text{ at } \theta_2}{I_{\gamma_1} \text{ at } \theta_2 \text{ gated by } \gamma_2 \text{ at } \theta_1}, \quad (1)$$

where the I_γ refers to the intensity of the γ-ray transition and γ_2 is a gating transition of a known multipolarity. The R_{DCO} values obtained with a gate on a stretched quadrupole (dipole) transition are ≈1.0(2.0) and ≈0.5(1.0) for stretched quadrupole and dipole transitions, respectively.

Information on the electric and magnetic nature of the transitions is obtained from the linear polarization (P) measurements. The linear polarization of γ rays depends on the polarization asymmetry (Δ_{asym}) and the polarization sensitivity, $Q(E_\gamma)$, by the relation $P = \Delta_{\mathrm{asym}}/Q(E_\gamma)$. The Δ_{asym} was determined using

$$\Delta_{\mathrm{asym}} = \frac{a(E_\gamma)N_\perp - N_\parallel}{a(E_\gamma)N_\perp + N_\parallel}, \quad (2)$$

where $N_\perp$ ($N_\parallel$) refers to the counts of the γ-ray photons scattered in the perpendicular (parallel) crystals of the clover detectors at 90° with respect to the reaction plane. The factor $a(E_\gamma)$ is a measure of the geometrical asymmetry, which corresponds to the ratio of the $N_\parallel$ and $N_\perp$ for the γ rays from an unpolarized source. The standard ^{152}Eu source was used to extract the value of $a(E_\gamma)$ and it was found to be close to unity for the present experimental setup. Further details of the matrices used for the Δ_{asym} measurements are given in Ref. [34].

The polarization sensitivities at different γ-ray energies were determined using the known stretched $E2$ transitions. The experimental Δ_{asym} values of these transitions were obtained using the technique discussed above. The corresponding linear polarization (P) values were calculated using the Klein-Nishina formula [47] and the angular distribution coefficients of the transitions, which were taken from the reference [38]. The resulting $Q(E_\gamma)$ values were plotted as a function of γ-ray energy and fitted using the equation [46,48]

$$Q(E_\gamma) = (CE_\gamma + D)Q_0(E_\gamma), \quad (3)$$

where $Q_0(E_\gamma)$ is known as the polarization sensitivity for an ideal Compton polarimeter, and is defined as

$$Q_0(E_\gamma) = \frac{(\alpha + 1)}{(\alpha^2 + \alpha + 1)} \quad (4)$$

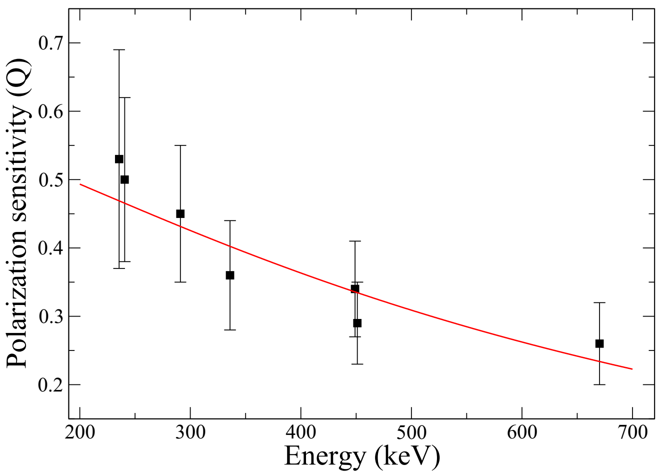

FIG. 1. Measurement of polarization sensitivity as a function of γ-ray energy. The solid (red) line represents the least-square fit of the data points with the function given in Eq. (3).

with $\alpha = E_\gamma/m_ec^2$, where E_γ is the energy of the γ-ray transition and m_ec^2 is the rest mass energy of the electron. The least-squares fit to the experimental $Q(E_\gamma)$ values, as shown in Fig. 1, results in $C = -0.00027(16)$ keV^{-1} and $D = 0.59(7)$.

The positive and negative values of the linear polarization indicate the electric and magnetic natures of the transition under consideration, respectively, while a near-zero value usually suggests a mixed multipolarity. In order to calculate the multipole mixing probability for a given transition, the experimental values of the R_{DCO} and the linear polarization (P) were compared with the corresponding theoretical values, which were calculated as outlined in the references [49,50]. The value 0.3 was considered for the spin alignment parameter (σ/J).

III. RESULTS

A. Level scheme

The level scheme of ^{215}Fr inferred from the present study is shown in Figs. 2 and 3. A total of 52 new transitions were identified and placed in the level scheme based on the γ-γ coincidence analysis. The placement of the new transitions extends the current level scheme up to spin $55/2\hbar$ and excitation energy 4.8 MeV. The spin-parity of the levels were assigned on the basis of the R_{DCO} and linear polarization measurements. The γ-ray energies, level energies, relative γ-ray intensity, the multipolarity of the γ-ray transitions, and the respective R_{DCO} and linear polarization values (where available) are listed in Table I. Figure 4 illustrates parts of the γ-γ coincidence spectrum in the gate of the 670-keV transition in different energy ranges. The spectra reveal several new transitions. The prompt and *early-delayed* coincidence relationships of these transitions were further utilized to ascertain their position in the level scheme.

The lower part of the level scheme (see Fig. 2) shows two sequences ("A" and "B") of $\Delta I = 2$ transitions, which are interconnected by the 700-, 479- and 319-keV transitions. $I^\pi = 9/2^-$ and $13/2^-$ for the ground state and the first excited state, respectively, are adopted from the earlier studies [36–38]. Further, negative parity is assigned to the states at 1121 and 1457 keV in sequence A based on the measured polarization values (see Table I) for the 451- and 336-keV transitions, respectively. The R_{DCO} values of the 700-, 479-, and 319-keV transitions indicate their $\Delta I = 1$ character. Further, positive values of the linear polarization for the 700- and 479-keV transitions suggest their $E1$ multipolarities, while a near-zero value of P for the 319-keV transition indicates its mixed $M1 + E2$ nature. The suggested $E1$ multipolarity of the 700- and 479-keV transitions would lead to the positive parity of the 1149- and 700-keV levels in sequence B. However, earlier studies had unambiguously assigned negative parity to the states in sequence B on the basis of the angular distribution measurements and the conversion-electron spectroscopy. Therefore, to find the true nature of the aforementioned interconnecting transitions and parity of the states in the sequence B, the multipole mixing ratios were determined. For this purpose, theoretical values of the R_{DCO} and polarization were extracted as a function of mixing ratio as discussed in Sec. II. The resulting theoretical contours along with the corresponding experimental values are shown in Fig. 5. It should be noted that each point on the contours has a specific value of mixing ratio. A comparison of the theoretical and the

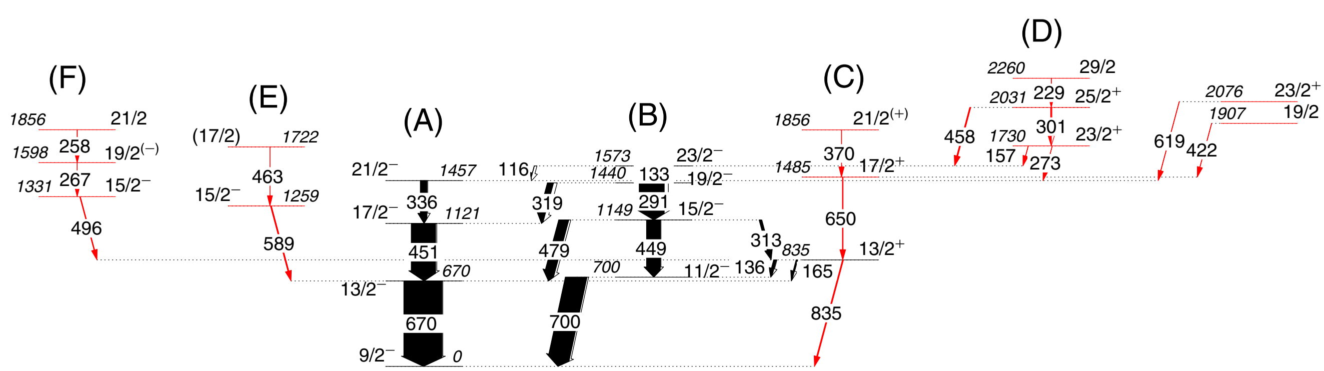

FIG. 2. Low-energy part of the level scheme of ^{215}Fr obtained from the present work. The levels and γ-ray transitions are labeled with their energies in keV. The widths of closed and open areas of the arrows correspond to the intensity of the γ rays and internal conversion electrons, respectively. The newly identified transitions and levels are marked in red color.

TABLE I. The table of γ-ray energies (E_γ), level energies (E_i), spin and parity of the levels, relative γ-ray intensities (I_γ), multipole mixing ratios, and assigned multipolarities of the γ-ray transitions from ^{215}Fr. The listed uncertainties in the γ-ray intensities and DCO ratios correspond to the statistical errors only. The systematic uncertainty in I_γ is about 5%.

E_γ (keV)[a]	E_i (keV)	J_i^π	I_γ	R_{DCO}	Polarization (P)	δ	Multipolarity
107.5	1813.5	$27/2^-$	17.1(3)	0.80(5)			$M1$[c]
111.3	3408.9	$41/2^+$	9.1(2)				
113.7	3014.3		3.2(2)				
115.7	1572.9	$23/2^-$	6.0(1)				
133.1	1572.9	$23/2^-$	143.0(17)	0.97(2)			$E2$[c]
133.2	1706.0	$25/2^-$	47.8(17)				$M1$[c]
135.6	835.4	$13/2^+$	68.5(11)	1.31(2)[b]			D
138.6	3207.5		3.8(2)				
150.4	1964.0	$31/2^-$	16.0(5)	0.99(2)			$E2$[c]
157.3	1730.2	$23/2^+$	5.3(1)	1.11(2)			D[d]
165.2	835.4	$13/2^+$	35.7(5)	0.97(2)			D[d]
193.8	3094.4	$39/2^{(-)}$	21.8(3)	1.15(4)			$E2$[c]
202.5	2016.0	$29/2^+$	315.2(35)	0.64(1)			$E1$[c]
219.2	1659.0	21/2	5.9(1)	0.57(1)			D
228.6	3297.5	43/2	10.1(2)	1.03(2)			Q
229.2	2260.4	29/2	2.6(3)	1.86(8)[b]			Q
235.6	2251.6	$33/2^+$	234.2(26)	1.05(2)	+0.39(9)		$E2$
236.6	4102.1	47/2	7.1(3)	1.13(2)			Q
240.6	1813.5	$27/2^-$	138.3(15)	0.99(2)	+0.50(12)		$E2$
244.8	2496.4	35/2	6.3(1)	0.62(2)			D
258.3	1856.4	21/2	5.3(1)	0.58(1)			D
262.0	3068.9	$39/2^-$	70.2(8)	2.03(6)[b]	+0.34(10)		$E2$
266.9	1598.1	$19/2^{(-)}$	3.5(1)	0.94(2)			Q
270.4	3679.3	(43/2)	4.4(2)	0.76(3)			$D+Q$
272.8	1730.2	$23/2^+$	1.5(1)				
276.9	4379.0	51/2	4.9(3)	0.93(2)			Q
277.5	2293.3	$29/2^+$	4.3(1)				
291.0	1439.8	$19/2^-$	655.5(69)	1.00(1)	+0.54(11)		$E2$
299.3	1448.0	(17/2)	1.1(1)				
301.0	2031.2	$25/2^+$	20.0(3)	0.54(3)	−0.36(18)		$M1$
313.4	1148.8	$15/2^-$	68.8(11)	1.19(1)	+0.32(16)		$E1$
318.6	1439.8	$19/2^-$	157.7(23)	0.53(1)	+0.07(5)	−9.9(19)	$M1+E2$
326.7	1448.0	(17/2)	11.8(2)	1.11(2)			D[d]
335.9	1457.2	$21/2^-$	175.5(26)	1.00(1)	+0.45(9)		$E2$
340.0	3408.9	$41/2^+$	28.5(4)	1.01(1)[b]	+0.30(12)		$E1$
367.7	1203.1	(13/2)	2.7(2)				
370.5	1855.7	$21/2^{(+)}$	5.0(2)	1.03(5)			Q
381.2	1838.4	25/2	5.0(2)	0.98(2)			Q
391.6	4770.6	55/2	4.2(3)	0.85(3)			Q
415.2	3484.1		20.6(9)				
416.2	1856.0	21/2	17.9(10)	0.63(3)			D
421.5	1906.7	19/2	5.1(1)	0.48(2)			D
449.0	1148.8	$15/2^-$	360.1(36)	1.99(1)[b]	+0.51(12)		$E2$
451.1	1121.3	$17/2^-$	637.8(65)	0.95(1)	+0.42(10)		$E2$
456.7	3865.6	43/2	13.7(5)	0.66(1)			D
458.3	2031.2	$25/2^+$	28.7(4)	1.07(6)[b]	+0.37(12)		$E1$
462.9	1721.8	(17/2)	2.3(2)	0.79(4)			$D+Q$
473.7	2046.6	27/2	10.1(2)	0.97(2)			Q
478.6	1148.8	$15/2^-$	258.0(38)	0.46(1)	+0.19(8)	−4.1(4)	$M1+E2$
479.8	2293.3	$29/2^+$	32.7(6)	1.03(5)[b]	+0.32(23)		$E1$
491.4	1948.6	25/2	3.3(1)	0.90(2)			Q
495.8	1331.2	$15/2^-$	18.5(4)	1.02(5)[b]	+0.23(14)		$E1$
499.6	1956.8	25/2	8.5(2)	0.87(2)			Q
503.1	1203.1	(13/2)	5.3(1)	0.95(4)[b]			D

TABLE I. (*Continued.*)

E_γ (keV)[a]	E_i (keV)	J_i^π	I_γ	$R_{\rm DCO}$	Polarization (P)	δ	Multipolarity
530.1	2343.6	29/2	8.0(2)	0.59(2)			D
532.9	1203.1	(13/2)	11.8(2)	0.89(2)			D[d]
551.8	1387.2	$15/2^-$	23.6(5)	1.11(4)[b]	+0.57(23)		$E1$
555.3	2806.9	$35/2^-$	109.4(13)	0.64(1)	+0.50(17)		$E1$
588.7	1258.9	$15/2^-$	25.1(4)	0.64(3)	−0.26(24)		$M1+E2$
589.4	3998.3	45/2	9.2(4)	0.90(3)			Q
619.2	2076.4	$23/2^+$	7.2(2)	0.56(1)	+0.67(25)		$E1$
630.0	2443.5	31/2	5.8(1)	0.93(2)			Q
636.8	2094.0		2.3(1)				
641.4	2214.3	25/2	7.5(2)	0.60(1)			D
649.0	2900.6	$35/2^-$	24.9(6)	0.54(1)	+0.37(20)		$E1$
649.8	1485.2	$17/2^+$	17.6(10)	2.02(4)[b]	+0.29(19)		$E2$
670.2	670.2	$13/2^-$	1000.0(71)	0.95(1)	+0.47(15)		$E2$
682.7	2139.9	23/2	4.5(1)	0.52(1)			D
687.5	2127.3	23/2	5.2(1)	1.03(3)			Q
699.8	699.8	$11/2^-$	556.0(56)	0.53(1)	+0.22(9)	−8.1(13)	$M1+E2$
717.0	1387.2	$15/2^-$	5.0(2)	0.47(1)	−0.50(32)		$M1$
780.8	1451.0	17/2	3.6(3)	0.97(4)			Q
817.3	3068.9	$39/2^-$	27.1(5)	1.12(5)	+0.86(36)		$E3$[e]
835.4	835.4	$13/2^+$	24.9(9)	1.77(4)[b]	−0.39(19)		$M2$
882.6	4291.5	45/2	6.8(4)	0.99(4)			Q
954.6	2768.1	$31/2^-$	11.2(2)	1.17(3)	+0.53(38)		$E2$
971.3	3222.9	$37/2^+$	9.5(2)	1.18(3)	+0.82(51)		$E2$
1080.8	2894.3	$31/2^-$	11.6(2)	1.23(3)	+0.57(48)		$E2$

[a]Uncertainties in γ-ray energies are up to 0.5 keV.
[b]In the gate of dipole ($\Delta I = 1$) transition. For all the remaining transitions, $R_{\rm DCO}$ values are calculated in the gate of quadrupole ($\Delta I = 2$) transitions.
[c]From intensity balance and coincidence relationships.
[d]$\Delta I = 0$ dipole transition.
[e]From γ-γ coincidence relationships.

experimental values of the $R_{\rm DCO}$ and polarization (P) for a given transition yields the value of mixing ratio. The deduced mixing ratios for the 700-, 479-, and 319-keV transitions are −8.1(13), −4.1(4), and −9.9(19), respectively, which correspond to a $\gtrsim$95% $E2$ component in all three transitions. The above values of the mixing ratios are also consistent with those reported in the earlier studies by Decman *et al.* [36] and Drigert *et al.* [38].

The γ-γ coincidence relationships suggest a few unobserved low-energy transitions in the proposed level scheme. The 116-keV γ ray is observed in coincidence with the 291- and 319-keV transitions, which indicates the presence of an unobserved 17-keV transition between the $21/2^-$ and $19/2^-$ states. Further, the coincidence relationship of the 291- and 451-keV transitions requires an unobserved 28-keV γ ray between the $15/2^-$ and $17/2^-$ levels at 1149- and 1121 keV, respectively. The intensity balance at the 1440-, 1149-, and 1121-keV levels also corroborates the presence of the above low-energy $M1$ transitions. An unobserved 30-keV transition was also reported by Decman *et al.* [36] between the 700- and 670-keV levels. The existence of this transition can be established by the coincidence between the 670- and 449-keV transitions. The double gated spectrum of the 670- and 291-keV transitions indicates a weak 449-keV transition, which is possible only if the unobserved 30-keV transition is present. However, the single gate of the 670-keV transition does not provide any conclusive evidence of the 449 keV, and hence for the unobserved 30-keV γ ray. This suggests that the 30-keV decay-branch of the 700-keV level is very weak, and hence the corresponding weak 449-keV transition in the gate of the 670-keV γ-ray is obscured by the presence of the intense 451-keV transition.

Further, a new 150-keV transition is observed in coincidence with all the earlier known transitions in the yrast sequence except the 202 keV. Following the $R_{\rm DCO}$ value of the 150-keV γ ray and the intensity balance at the 2016- and 1814-keV levels, a tentative $31/2^-$ state is proposed at 1964 keV. The coincidence relationship of the new 150 keV and the 236-keV γ rays requires an unobserved transition of 52 keV between the $29/2^+$ and the new $31/2^-$ levels. However, the ordering of the new 150 keV and the unobserved 52-keV transitions is uncertain. In this case, an alternative level could be at 1866 keV with $I^\pi = 25/2^+$.

A new positive-parity sequence "C" of $\Delta I = 2$ transitions viz. 835-, 650- and 370 keV is established. The above transitions are placed in a cascade on the basis of coincidences and intensity considerations. The $13/2^+$ state at 835 keV was known from earlier work [36–38]. The spin and parity of this state were proposed using intensity balance [37] and angular distribution measurements for the 313- and 135-keV

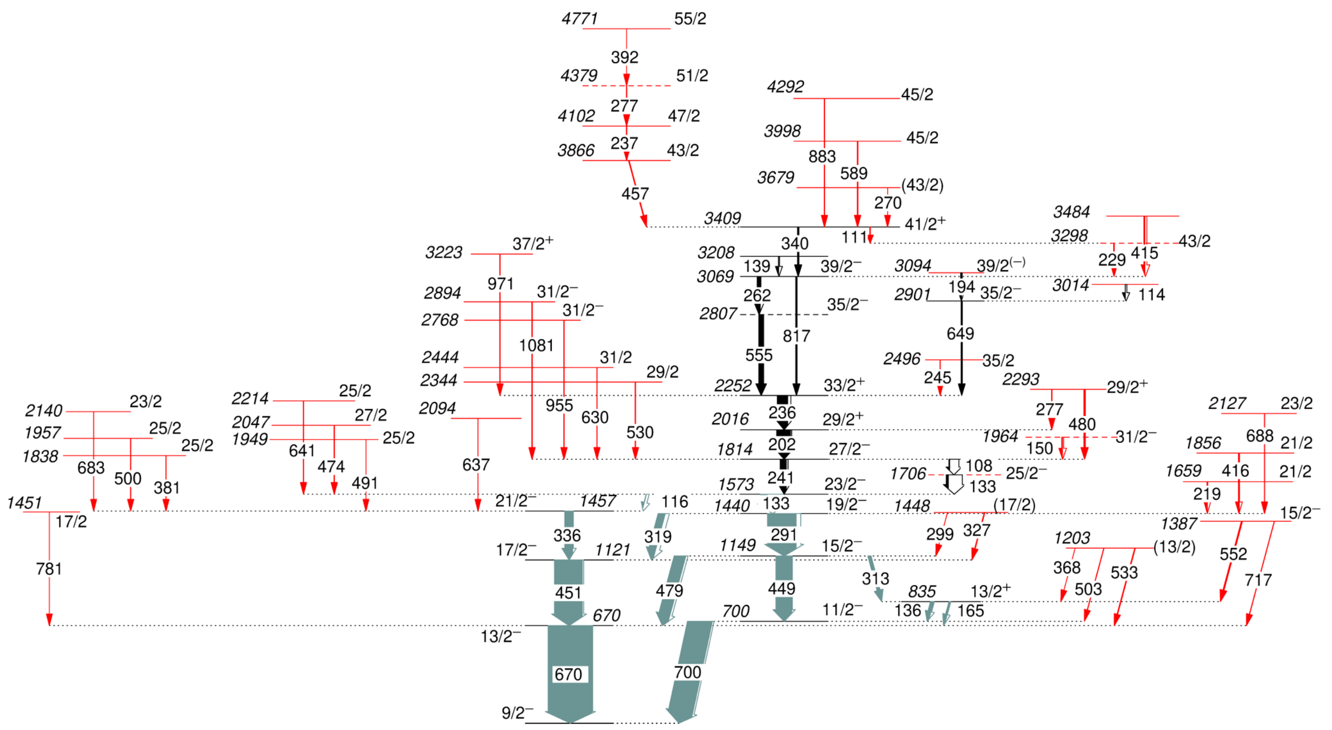

FIG. 3. Remaining part of the level scheme of ^{215}Fr obtained from the present work. The levels and γ-ray transitions are labeled with their energies in keV. The widths of closed and open areas of the arrows correspond to the intensity of the γ rays and internal conversion electrons, respectively. The newly identified transitions and levels are marked in red color and the transitions which are already presented in Fig. 2 are shown in turquoise color. The levels shown with a dashed line are tentative.

transitions [38]. A new 835-keV transition which de-excites the $13/2^+$ state directly to the ground state is identified in the present work. The $R_{\rm DCO}$ and linear polarization values (Table I) unequivocally suggest its M2 multipolarity, which in turn confirms $I^\pi = 13/2^+$ assignment of the state at 835 keV. Further, the linear polarization of the 650-keV transition clearly indicates its electric nature and hence, $I^\pi = 17/2^+$ is assigned to the state at 1485 keV. The parity of the 1856-keV state could not be determined owing to the weak 370-keV γ ray which de-excites it.

Figure 6 illustrates the γ rays in coincidence with (a) the 552-, 717- (inset), and (b) the 496-keV transitions. It is evident from Fig. 6(a) that the 552-keV transition is in coincidence with all the transitions below the $13/2^+$ state. Therefore, the 552-keV transition is placed above the $13/2^+$ state. This

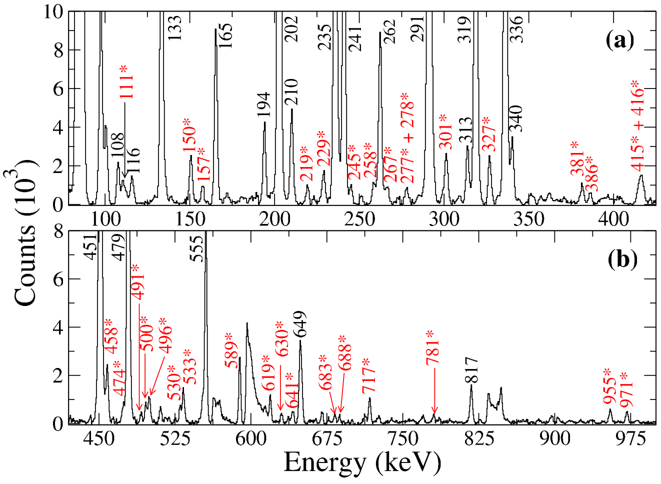

FIG. 4. γ-γ coincidence spectrum with the gate on the known 670-keV γ ray in ^{215}Fr showing the transitions (a) up to 425 keV and (b) in the 425–1000 keV energy range. The new transitions identified from the present work are labeled with an asterisk and red color.

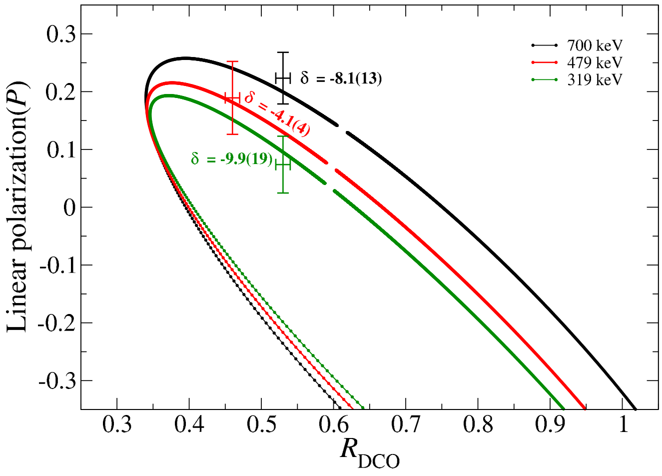

FIG. 5. Mixing ratio contour plots illustrating the theoretical values of $R_{\rm DCO}$ and polarization (P) for the linking transitions, 700-, 479- and 319 keV, between the sequences A and B. The corresponding experimental values are marked as data points with error bars in the same color.

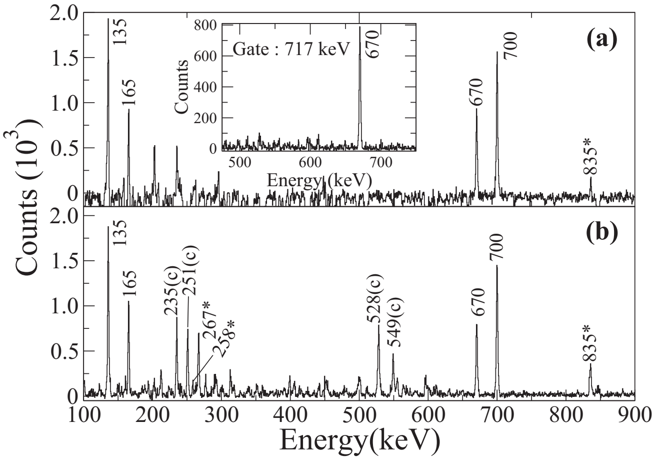

FIG. 6. Gamma-gamma coincidence spectra depicting transitions in gate of the (a) 552- and 717 keV (inset), and (b) 496-keV transitions. The new transitions are marked with asterisk and the transitions labeled with "c" are contaminates from ^{216}Fr.

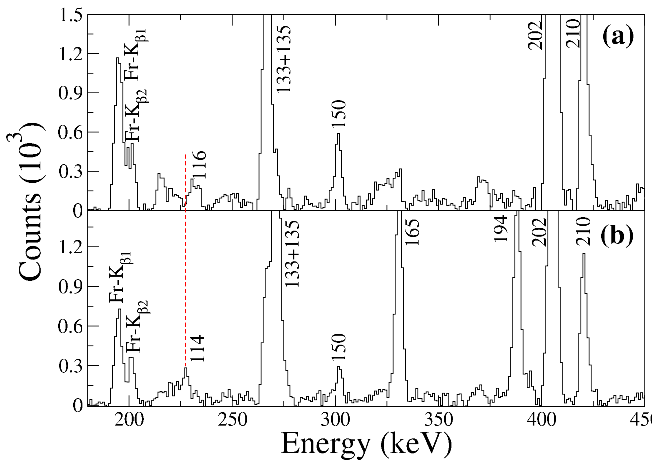

FIG. 7. Gamma-ray spectra illustrating transitions in coincidence with the (a) 194- and, (b) 649-keV transitions.

introduces a new state at 1387 keV. Based on the R_{DCO} and linear polarization values of the 552-keV γ ray, $I^{\pi} = 15/2^{-}$ is assigned to the proposed state. Further, a new 717-keV transition is also identified, which originates from the same state and feeds directly to the yrast $13/2^{-}$ state. It can be seen that only the 670-keV γ ray is present in the gate of the 717 keV [see inset of Fig. 6(a)]. The deduced M1 multipolarity of the 717-keV transition confirms the proposed spin-parity, $I^{\pi} = 15/2^{-}$, of the 1387-keV state. Similarly, Fig. 6(b) depicts transitions pertaining to the sequence "F" of the level scheme. Similar analysis techniques were used to establish remaining states in the level scheme as shown in Figs. 2 and 3.

The proposed level scheme also reveals several $\Delta I = 0$ dipole transitions, viz. 165-, 157-, 278-, 327-, and 533 keV. It may be noted that a pure $\Delta I = 0$ dipole transition has almost identical angular correlations as a stretched quadrupole ($\Delta I = 2$) one [51]. The R_{DCO} value for the 157-keV transition is identical to that expected for a quadrupole transition (Table I). If the 157-keV transition is indeed a $\Delta I = 2$ transition, it would most likely have an $E2$ multipolarity, and hence $I^{\pi} = 27/2^{-}$ assignment would have been more appropriate for the state at 1730 keV. This assignment would then have resulted in $M3$ multipolarity of the 273-keV γ ray, which depopulates the same state to the $21/2^{-}$ level in the sequence "A". Such low-energy $M3$ transitions are highly hindered. The above discussion and the extracted R_{DCO} value for the 157-keV transition suggest its $\Delta I = 0$ dipole nature. Further, the deduced multipolarities of the 458- and 301-keV transitions confirm the $I^{\pi} = 23/2^{+}$ assignment to the 1730-keV level. Similar arguments were considered to ascertain the dipole ($\Delta I = 0$) nature of the other transitions mentioned above.

The present analysis also suggests a few modifications to the earlier reported level structures above the $33/2^{+}$ state at 2251 keV [36–38]. Schulz *et al.* [37] had reported a cascade of three consecutive transitions, viz., 194, 114, and 649 keV, which feeds the $33/2^{+}$ state. It is observed from the present data that the 114-keV γ ray is in coincidence with the 649-keV transition [Fig. 7(b)] but not the 194-keV γ ray [Fig. 7(a)]. Hence, both 194- and 114-keV transitions are placed above the 649-keV transition. Also, it was noticed that the multipolarity of the 649-keV transition was not consistent among the earlier works [37,38]. Schulz *et al.* [37] have assigned tentative $E1$ multipolarity, while a mixed $M1 + E2$ assignment was made by Drigert *et al.* [38]. Based on the R_{DCO} and linear polarization measurements (Table I), we unambiguously assign $E1$ multipolarity to the 649-keV transition.

Figure 8 depicts several new transitions in *early* coincidence of the 555-keV γ ray. A total of ten new transitions were placed above the $39/2^{-}$ isomeric state at 3069 keV, and constitute nine new levels. The placement of the new transitions extends the level scheme up to 4770 keV and $55/2\hbar$. Following the intensity and coincidence relations, a new sequence of weak $\Delta I = 2$ transitions, viz., 237, 277, and 392 keV, is established. However, ordering of the 277-

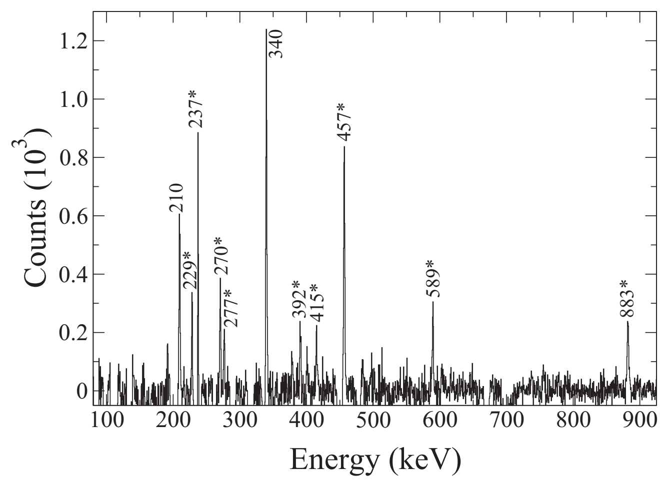

FIG. 8. γ-ray spectra illustrating *early* transitions in the gate of the 555-keV γ ray within the 50–200 ns time window. The new transitions are marked with an asterisk.

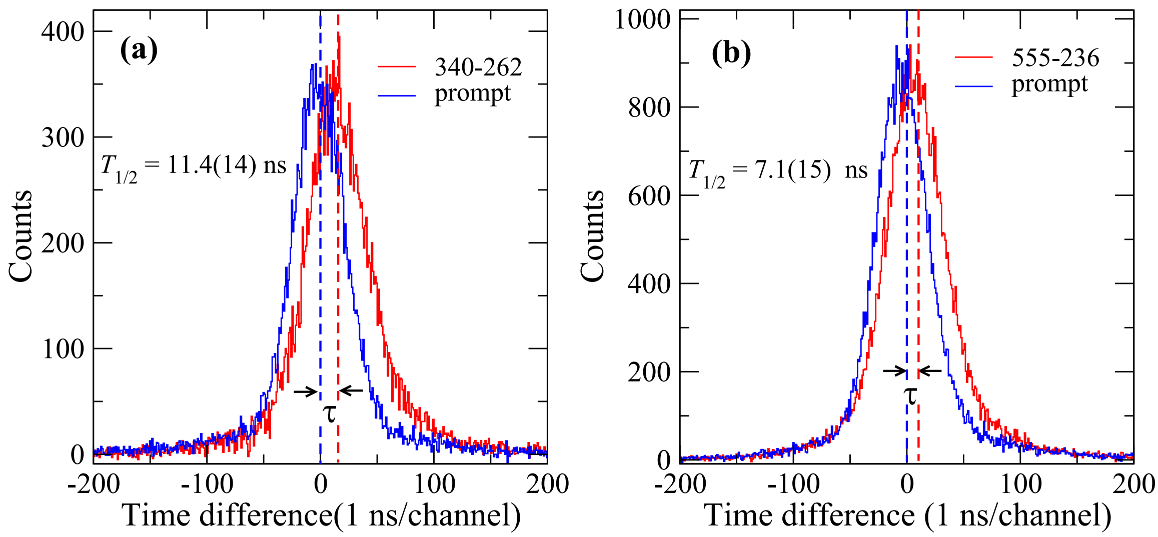

FIG. 9. Time-difference spectra (red) of the (a) 340-, 262-keV and the (b) 555-, 236-keV transitions illustrating the half-lives of the $39/2^-$ and $33/2^+$ states, respectively. The spectra in blue color illustrate the time difference of the similar energy prompt transitions.

and 392-keV transitions cannot be confirmed. The proposed sequence feeds the $39/2^-$ isomeric state via new 457- and 340-keV consecutive transitions.

The remaining level structure is also established using the prompt and *early-delayed* coincidence relationships, intensity balance, R_{DCO}, and the polarization measurements as shown in Figs. 2 and 3. In addition to the previously reported 210-keV γ ray [37] and tentative 519-keV γ ray [38], some of the newly identified γ rays, viz., 351, 362, 386, and 712 keV could not be placed in the level scheme. The 210-keV γ ray is observed in coincidence with all the transitions up to the $39/2^-$ isomeric state in the present work. However, its placement in the level scheme could not be ascertained, mainly because the present data indicate doublet structure of the 210-keV transitions.

B. Revisiting isomers in ^{215}Fr

Prior to the present study, Decman *et al.* [36] and Schulz *et al.* [37] had reported several isomers in ^{215}Fr. The reported half-lives of the $39/2^-$ isomer at 3069 keV are notably different. Also, Schulz *et al.* [37] reported a $27/2^-$ isomer with $T_{1/2} = 2.1(14)$ ns at 1814 keV, while Decman *et al.* [36] did not assign any value of half-life to this state. In order to ascertain the half-lives of the above states and to search for new isomers in ^{215}Fr, centroid-shift analysis was performed. Figure 9(a) illustrates the time-difference spectrum of the 340- and 262-keV γ-ray transitions which feed and deexcite the $39/2^-$ isomer, respectively. It is compared with the time-difference spectrum of the similar energy prompt transitions. This leads to $T_{1/2} = 11.4(14)$ ns. The total error in the half-life was obtained by combining the statistical and systematic uncertainties in quadrature. The statistical uncertainty corresponds to the error in the centroids of the prompt and delayed distributions. The systematic error includes contributions from the discrete binning along the time axis and the uncertainty arising due to shift in the centroid of the prompt distribution of two similar energy transitions. The deduced half-life, for the $39/2^-$ state at 3069 keV, is in agreement with $T_{1/2} = 14.6(14)$ ns measured by Schulz *et al.* [37]. It may also be noted that the $T_{1/2} = 33(5)$ ns was reported by Decman *et al.* [36] for the same state. The higher value may be attributed to the contribution from the feeding of the $I^\pi = 47/2^+$ isomeric state [$T_{1/2} = 23(2)$ ns] [37] to the $39/2^-$ state. This feeding was not observed in the work of Decman *et al.* [36]. For the $I^\pi = 33/2^+$ state, $T_{1/2} = 7.1(15)$ ns is obtained using the centroid-shift analysis of the 555- and 236-keV transitions as depicted in Fig. 9(b). The deduced half-life is in agreement with the earlier reported values [36,37].

Figure 10 illustrates the centroid-shift analysis of the 236- and 241-keV transitions, which results in a cumulative half-

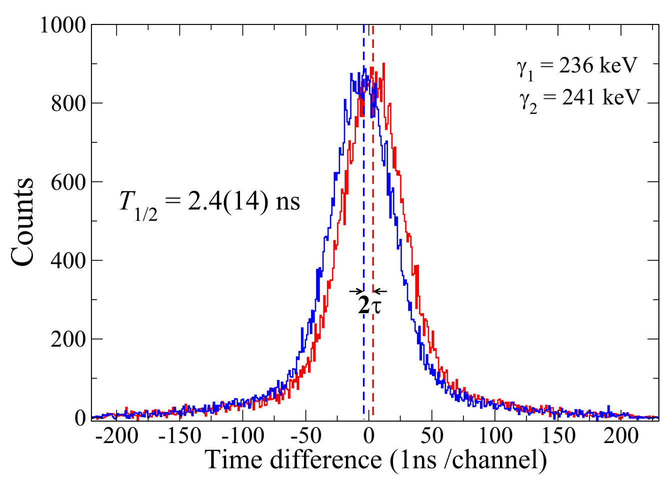

FIG. 10. Centroid-shift analysis illustrating the cumulative half-life of the yrast $29/2^+$ and $27/2^-$ states. The red (blue) spectra are generated using γ_1 (γ_2) as start and γ_2 (γ_1) as stop signal. It is assumed that the time response of the detectors is the same for both the transitions under consideration.

TABLE II. Comparison of the half-lives of the isomeric states obtained from the present work and those reported in the literature.

	$T_{1/2}$ (ns)		
Isomeric level	Present study	From Ref. [37]	From Ref. [36]
$19/2^-, 21/2^-, 23/2^-$	3.2(15)[a]	3.5(14)[b]	4(2)[a]
$27/2^-$		2.1(14)	
$29/2^+$	2.4(14)	5.5(14)	3(2)
$33/2^+$	7.1(15)	5.5(14)	5(2)
$39/2^-$	11.4(14)	14.6(14)	33(5)

[a]Cumulative half-life of the $19/2^-, 21/2^-, 23/2^-$ states.
[b]Half-life of the $23/2^-$ state.

life of 2.4(14) ns for the $29/2^+$ and $27/2^-$ states. Further, the time-difference spectra of the γ-ray transitions depopulating and feeding the $27/2^-$ state do not yield any half-life. The above analysis suggests that the deduced cumulative half-life is mainly associated with the $29/2^+$ level. This is consistent with the study by Decman *et al.* [36], wherein $T_{1/2} = 3(2)$ ns was reported for the $29/2^+$ state while the $27/2^-$ state was not reported to be isomeric. It may be noted that Schulz *et al.* [37] had reported $T_{1/2} = 5.5(14)$ and 2.1(14) ns for the $29/2^+$ and $27/2^-$ states, respectively. If the $27/2^-$ state is indeed isomeric, then the cumulative half-life of the above states would be larger than that obtained in the present work.

Further, a cumulative half-life of 3.2(15) ns is determined for the $23/2^-$, $21/2^-$, and $19/2^-$ states using the centroid-shift analysis of the 241- and 291-keV transitions, which is found to be consistent with the earlier reported values [36,37]. It may also be noted that the time response of the γ-ray transitions and background corrections are taken into account while extracting the half-lives using the centroid-shift analysis. The deduced half-lives are compared with those reported in the literature in Table II.

As mentioned earlier, Schulz *et al.* [37] had also reported a longer lived [$T_{1/2} = 23(2)$ ns] $47/2^+$ isomer at 3462 keV, which was reported to deexcite via 45- and 210-keV transitions to the $41/2^-$ state at 3208 keV [37]. In the present work, we could not observe the 45-keV γ ray (due to the limitation of the experimental setup) and the placement of the 210-keV γ ray could not be established. Therefore, the $47/2^+$ isomeric state also could not be confirmed.

IV. DISCUSSION

Three consecutive high-spin studies of ^{215}Fr were reported earlier [36–38], wherein the yrast and a few near-yrast states up to $47/2\hbar$ and 3462 keV excitation energy were established. In-beam studies were performed using α-γ, γ-γ, and conversion-electron spectroscopy. Decman *et al.* [36] and Schulz *et al.* [37] had reported a total of six high-spin isomers. The half-lives of the isomers were measured using pulsed beam and the centroid-shift analysis. Also, the *g*-factors were measured for the isomeric states by Decman *et al.* [36] using the ^{204}Hg(^{15}N, $4n$)^{215}Fr reaction. The reported level structures were interpreted in the framework of the shell model and deformed independent-particle model.

As indicated in Sec. I and also by the proposed level scheme, the states in ^{215}Fr appear to be mainly governed by the single-particle structure, where the shell-model approach prevails. Therefore, detailed shell-model calculations were performed and are discussed in the following section. In addition to the quantal description of the yrast and near yrast states, *rotational* interpretation of the noncollectively rotating system [52] is also discussed. For this, the level energies are plotted as a function of $I(I+1)$ and structure of the yrast line is compared with the neighboring $N = 128$ isotones, which provides insights into the level structure in different energy and spin regimes.

A. Shell-model calculations and interpretation of high-spin levels

Large-scale shell-model calculations were performed using the effective interaction which was derived from the CD-Bonn NN potential employing the $V_{\text{low-}k}$ renormalization approach [53]. Further, the diagonalization of the matrices was done using the shell-model code KSHELL [54]. The chosen valence space consisted of the protons in the $0h_{9/2}$, $1f_{7/2}$, $0i_{13/2}$, $1f_{5/2}$, $2p_{3/2}$, and $2p_{1/2}$ orbitals and the neutrons in the $1g_{9/2}$, $0i_{11/2}$, $0j_{15/2}$, $2d_{5/2}$, $3s_{1/2}$, $1g_{7/2}$, and $2d_{3/2}$ orbitals. The calculations were unrestricted, allowing all the valence nucleons (five protons and two neutrons) outside the ^{208}Pb core to occupy any orbital in the defined valence-space without any truncation.

Figure 11 presents a comparison between the experimental and the predicted excitation energies of the yrast and near-yrast states. It is evident from the figure that the experimental results are in reasonably good agreement (to within 250 keV) with the calculations, except for the $39/2^-$ state which is underestimated by 416 keV. The dominant configuration for the low-lying negative parity states up to $I^\pi = 25/2^-$ is $\pi(h^5_{9/2}) \otimes \nu(g^2_{9/2})$. In addition, the second and third dominant configurations of the $13/2^-$, $15/2^-$, $17/2^-$, $19/2^-$, $21/2^-$, and $23/2^-$ states are $\pi(h^3_{9/2}f^2_{7/2}) \otimes \nu(g^2_{9/2})$ and $\pi(h^3_{9/2}i^2_{13/2}) \otimes \nu(g^2_{9/2})$, respectively, which introduce sufficient amount of proton-configuration mixing and explain the large $E2$ transition strengths as shown in Table III.

The low-lying sequences A and B, together with the linking transitions, viz., 700, 479, and 319 keV (Fig. 2), demonstrate one of the interesting aspects of this nucleus. As discussed in Sec. III, the inter-connecting transitions ($\Delta I = 1$) are found to be of mixed $M1 + E2$ character with dominant ($\gtrsim$95%) $E2$ component. In this respect, ^{215}Fr presents a unique example of near-spherical nucleus in which such high $E2$ mixing is observed. Table III lists the transition strengths obtained using the shell-model calculations. The mixing ratios (δ_{SM}) are deduced theoretically [55,56] using $B(E2)$ and $B(M1)$ rates obtained from the shell-model calculations and the corresponding experimental γ ray energies. It is observed that the calculated mixing ratio for the 479-keV transition is in relatively good agreement with the experimentally observed value. Only a lower limit for the mixing ratio of the 700-keV transition could be obtained (see Table III),

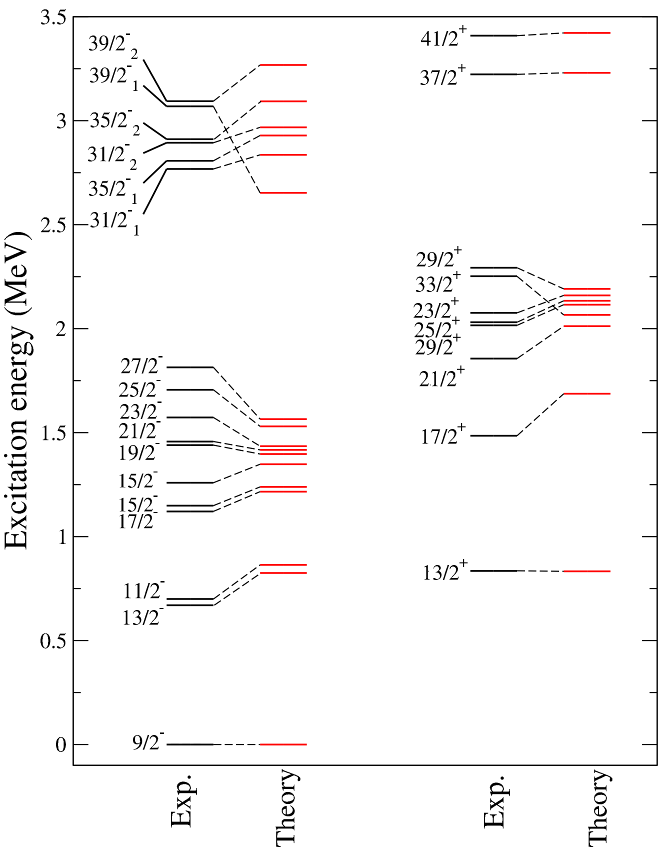

FIG. 11. The comparison of the experimental results with the shell-model calculations. Only the yrast and near-yrast levels for which spin-parities are deduced in the current work are considered for the comparison. Experimental excitation energy of the $35/2^-_2$ level is shifted by 10 keV for readability of the plot.

while a smaller mixing of $E2$ component is predicted for the 319-keV transition.

The dominant $E2$ component in the interconnecting transitions can also be understood using a semiempirical approach. The ground state, $I^\pi = 9/2^-$, and the low-lying negative-parity states (sequences A and B) in ^{215}Fr can be described as the $h_{9/2}$ proton weakly coupled to the even-even ^{214}Rn and ^{216}Ra core [36–38,57]. However, for further discussion, we consider only the ^{214}Rn core. The low-lying $0^+ - 8^+$ states in ^{214}Rn are associated with the $\pi(h^4_{9/2}) \otimes \nu(g^2_{9/2})$ configuration [18]. The $I'(2^+ - 8^+) \otimes h_{9/2}$ will lead to a multiplet of states, among which only the yrast and near-yrast states could be accessed from heavy-ion fusion-evaporation reactions. This is reflected in the sequences A and B in which the $11/2^-$, $13/2^-$ $(2^+ \otimes h_{9/2})$; $15/2^-$, $17/2^-$ $(4^+ \otimes h_{9/2})$; and $19/2^-$, $21/2^-$ $(6^+ \otimes h_{9/2})$ states are observed. With these configurations, the dominant $E2$ nature of the $11/2^- \to 9/2^-$ (700 keV), $15/2^- \to 13/2^-$ (479 keV), and $19/2^- \to 17/2^-$ (319 keV) can be explained as the transitions arising mainly between the 6^+, 4^+, 2^+, and 0^+ states of ^{214}Rn. Even the level energies of the ($13/2^-$, $11/2^-$), ($17/2^-$, $15/2^-$), ($19/2^-$, $21/2^-$), and ($23/2^-$, $25/2^-$) are nearly identical to the level energies of 2^+, 4^+, 6^+, and 8^+ levels of ^{214}Rn, respectively. The resulting sequences give the impression of highly decoupled bands

TABLE III. Calculated transition strengths for the selected transitions in ^{215}Fr are listed. The calculations were performed using $V_{\text{low-}k}$ effective interaction with $e_\pi = 1.5e$; $e_\nu = 0.5e$ and $g_s^{\text{eff}} = g_s^{\text{free}}$. For the three transitions, viz., 700, 479, and 319 keV, where experimental mixing ratios (δ) were known, δ_{SM} is deduced from the respective shell-model $B(E2)$ and $B(M1)$ rates and the corresponding E_γ^{exp} [55,56].

$J_i^\pi \to J_f^\pi$	E_γ^{exp} (keV)	$\sigma\lambda$	$B(\sigma\lambda)$ ($e^2\text{fm}^{2\lambda}$ or $\mu_0^2\text{fm}^{(2\lambda-2)}$)[a]	δ_{SM}
$11/2^-_1 \to 9/2^-_1$	699.8	$M1$	$<1.0 \times 10^{-3}$	< -3.8
		$E2$	4.33×10^2	
$13/2^-_1 \to 9/2^-_1$	670.2	$E2$	5.62×10^2	
$15/2^-_1 \to 11/2^-_1$	449.0	$E2$	3.27×10^2	
$15/2^-_1 \to 13/2^-_1$	478.6	$M1$	1.0×10^{-3}	-1.54
		$E2$	1.49×10^2	
$17/2^-_1 \to 13/2^-_1$	451.1	$E2$	5.61×10^2	
$19/2^-_1 \to 15/2^-_1$	291.0	$E2$	2.43×10^2	
$19/2^-_1 \to 17/2^-_1$	318.6	$M1$	1.6×10^{-2}	-0.13
		$E2$	3.7×10^1	
$21/2^-_1 \to 17/2^-_1$	335.9	$E2$	3.72×10^2	
$23/2^-_1 \to 19/2^-_1$	133.1	$E2$	2.10×10^2	
$39/2^-_1 \to 33/2^+_1$	817.3	$E3$	6.08×10^3	

[a]Units correspond to transition strength of electric and magnetic transitions, respectively.

arising from the $h_{9/2}$ orbital, as commonly observed in deformed nuclei. Similar structures have also been observed in ^{217}Ac [58], which is the isotone of ^{215}Fr.

The low-lying positive-parity states in the sequence C, viz., $13/2^+$, $17/2^+$, and $21/2^{(+)}$, are associated with the $\pi(h^4_{9/2}, i^1_{13/2}) \otimes \nu(g^2_{9/2})$ configuration, which may also be understood by the coupling of the $i_{13/2}$ proton to the 0^+, 2^+, and 4^+ states of the ^{214}Rn core.

Similar to the low-lying states discussed above, the structure of the higher-lying levels in ^{215}Fr can also be qualitatively understood as resulting from the coupling of the odd proton to the ^{214}Rn core. It was noticed that an isomeric 13^- [$T_{1/2} = 3.7(3)$ ns] [59] state at 2676 keV in ^{214}Rn decays via two branches: one with a 748 keV $E3$ transition to a 10^+ isomeric state ($T_{1/2} = 0.90(21)$ ns) at 1928 keV and another via a 282 keV $E2$ transition to an intermediate 11^- state at 2395 keV. A similar decay pattern is observed for the isomeric $39/2^-$ state [$T_{1/2} = 11.4(14)$ ns] at 3069 keV in ^{215}Fr (see Fig. 3). This state decays to the $33/2^+$ isomeric state [$T_{1/2} = 7.1(15)$ ns] via the 817 keV $E3$ transition and to the 2807 keV intermediate state ($35/2^-$) via the 262 keV $E2$ transition. The $33/2^+$, $35/2^-$, and $39/2^-$ states in ^{215}Fr can be thought of as arising from coupling of the proton in the $i_{13/2}$ orbital to the 10^+, 11^-, and 13^- states in ^{214}Rn, respectively. This is supported by the configurations suggested (see Table IV) by the shell-model calculations. The similar arguments are valid if a ^{216}Ra core is considered, in which the 10^+ [$T_{1/2} = 0.6(1)$ ns], 11^-, and 13^- [$T_{1/2} = 0.96(20)$ ns] states are known at 2026, 2335, and 2679 keV, respectively.

The $33/2^+$ level in ^{215}Fr may also be understood by addition of an extra $h_{9/2}$ proton to the known 13^- level

TABLE IV. Configurations of the states above the $25/2^-$ level in ^{215}Fr. Only the dominant configurations are reported except for the $33/2^+$ isomeric state, for which the second dominant configuration is also listed. A related explanation can be found in the text below.

State	SM (MeV)	Configuration	Partition %
$27/2^-_1$	1.565	$\pi(h^5_{9/2}) \otimes \nu(i^1_{11/2}g^1_{9/2})$	38
$29/2^+_1$	2.115	$\pi(h^4_{9/2}i^1_{13/2}) \otimes \nu(g^2_{9/2})$	38
$31/2^-_1$	2.836	$\pi(h^5_{9/2}) \otimes \nu(i^1_{11/2}g^1_{9/2})$	51
$31/2^-_2$	2.968	$\pi(h^5_{9/2}) \otimes \nu(g^2_{9/2})$	30
$33/2^+_1$	2.066	$\pi(h^5_{9/2}) \otimes \nu(i^1_{11/2}j^1_{15/2})$	25
		$\pi(h^4_{9/2}i^1_{13/2}) \otimes \nu(i^1_{11/2}g^1_{9/2})$	22
$35/2^-_1$	2.929	$\pi(h^4_{9/2}i^1_{13/2}) \otimes \nu(g^1_{9/2}j^1_{15/2})$	51
$35/2^-_2$	3.093	$\pi(h^5_{9/2}) \otimes \nu(i^1_{11/2}g^1_{9/2})$	65
$37/2^+_1$	3.230	$\pi(h^4_{9/2}i^1_{13/2}) \otimes \nu(i^1_{11/2}g^1_{9/2})$	52
$39/2^-_1$	2.653	$\pi(h^4_{9/2}i^1_{13/2}) \otimes \nu(i^1_{11/2}j^1_{15/2})$	65
$39/2^-_2$	3.268	$\pi(h^4_{9/2}f^1_{7/2}) \otimes \nu(g^2_{9/2})$	68
$41/2^+_1$	3.422	$\pi(h^4_{9/2}i^1_{13/2}) \otimes \nu(i^1_{11/2}g^1_{9/2})$	56

in ^{214}Rn [18,27]. The 13^- state has a mixed configuration with $\pi(h^4_{9/2}) \otimes \nu(i^1_{11/2}j^1_{15/2})$ carrying the dominant contribution. The coupling of the $h_{9/2}$ proton to this configuration leads to the most dominant configuration for the $33/2^+$ state in ^{215}Fr as predicted by the shell-model calculations (see Table IV). The structure of the $33/2^+$ state is mainly governed by two dominant configurations with almost equal parentage (see Table IV). The mixed configuration of the $33/2^+$ state facilitates its decay via the enhanced $E3$ transition (817 keV) as discussed below. If only the first configuration, $\pi(h^5_{9/2}) \otimes \nu(i^1_{11/2}j^1_{15/2})$, of the $33/2^+$ state is considered then the $39/2^- \rightarrow 33/2^+$ transition would lead to a "spin-flip" $(\pi i_{13/2} \rightarrow h_{9/2})$ $E3$ transition [30,31]. As mentioned in Sec. I, the $B(E3)$ rates corresponding to such transitions are typically of the order of 3–5 W.u., which are to be compared with the experimentally observed value (38.5 W.u). The presence of the second configuration, $\pi(h^4_{9/2}i^1_{13/2}) \otimes \nu(i^1_{11/2}g^1_{9/2})$, in the wave function of the $33/2^+$ state enables the $\nu(j_{15/2} \rightarrow g_{9/2})$ transition in addition to the "spin-flip" transition discussed above. The $j_{15/2}$ and $i_{13/2}$ orbitals are known to have a tendency to mix with the 3^- octupole phonon of the ^{208}Pb core. Therefore, the $\nu(j_{15/2} \rightarrow g_{9/2})$ and $\pi(i_{13/2} \rightarrow f_{7/2})$ single-particle transitions are relatively faster [52]. The above arguments support the decay of the $39/2^-$ state via the enhanced 817 keV $E3$ transition. The smaller calculated value of the transition strength (2.2 W.u.) for the 817-keV transition may be ascribed to the fact that the shell-model calculations do not include the mixing of the 3^- octupole phonon.

The 11^- state in ^{214}Rn [18,27] has $[\pi(h^3_{9/2}i^1_{13/2})_{11^-} \otimes \nu(g^2_{9/2})_{0^+}]_{11^-}$ configuration. Addition of an extra proton in the $h_{9/2}$ orbital to this configuration predicts a $29/2^+$ state in ^{215}Fr with $[\pi(h^4_{9/2}i^1_{13/2})_{29/2^+} \otimes \nu(g^2_{9/2})_{0^+}]_{29/2^+}$ configuration. The $29/2^+$ state is indeed present in the level scheme of ^{215}Fr at 2016 keV. The shell-model calculations also predict the same state at 2115 keV (see Table IV). This state decays to the $27/2^-$ level via the 202-keV $E1$ transition. It can be seen

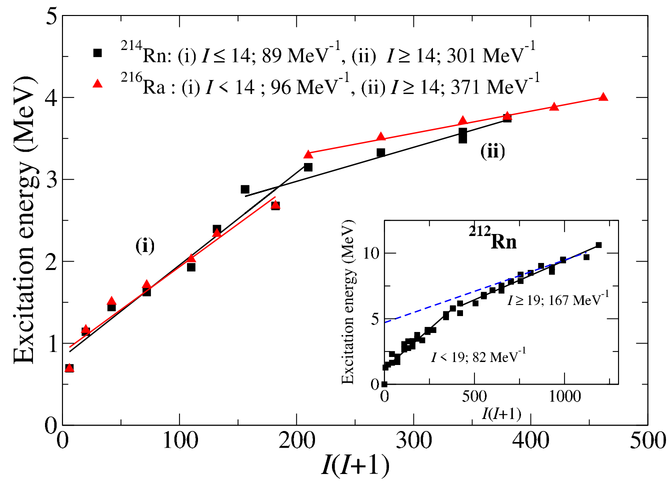

FIG. 12. Plot of the excitation energies of the yrast and near-yrast states versus $I(I+1)$ in ^{214}Rn, ^{216}Ra, and ^{212}Rn (in the inset). The information of the excited states in these nuclei is obtained from the Refs. [18,27,28,60]. The dashed line in the inset corresponds to the rigid body MOI for ^{212}Rn, which is drawn to coincide with the upper part of the plot.

from Table IV that there is a change in the orbitals occupied by both protons and neutrons for the $29/2^+$ and the $27/2^-$ states, which probably encounters inhibition in the decay of the $29/2^+$ state. A longer-lived $29/2^+$ isomer ($T_{1/2} = 740$ ns) has also been reported in ^{217}Ac ($N = 128$ isotone) at almost the same excitation energy [58].

B. Structure of the yrast line

The shape of the yrast line delineates the nuclear structure. Therefore, various spin regions could be defined in the yrast line corresponding to different nuclear structure phenomena. In particular, a rapid increase in the classical moment of inertia ("back-bending") with rotational frequency was observed at $I \approx 15$–$20\hbar$ in many even-even rare-earth nuclei [61]. This effect is explained in terms of the "pairing correlations" [52]. At high rotational frequency, one or more of the high-j nucleon pairs break due to the Coriolis antipairing effect, and the nucleus suddenly gains angular momentum from the alignment of the high-j pair of particles. This leads to a sudden rise in the moment of inertia (MOI) towards the rigid body value. This is reflected in the slope of the yrast line approaching the moment of inertia (MOI) of the rigid body value. A similar behavior of the yrast line is also observed in the nonrotational $N = 126$, 128 isotones with somewhat different explanation [38,62].

Figure 12 illustrates the distribution of excitation energies of the yrast and near-yrast states as a function of $I(I+1)$ in ^{214}Rn and ^{216}Ra [18,27,28], which are the isotones of ^{215}Fr. The yrast states which originate from the single-particle excitations (independent-particle motion) are expected to obey, on average, the relation appropriate to that of the rigid rotor [38,52]. Therefore, the points illustrating the yrast line are fitted with the expression of rotational energy, $E(I) = \frac{\hbar^2}{2\mathcal{J}_{\text{eff}}} I(I+1)$, where $\mathcal{J}_{\text{eff}}$ is the effective rigid body MOI. Interestingly,

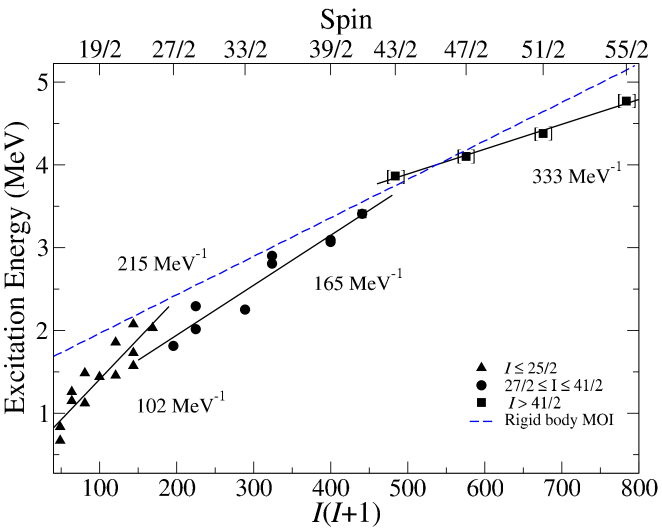

FIG. 13. Plot of the excitation energies of the yrast and near-yrast states versus $I(I+1)$ product in ^{215}Fr. The data points shown in brackets correspond to the states in $\Delta I = 2$ sequence with $I > 41/2\hbar$. The spins of these states are not known. All other states under consideration have firm spin-parity assignment. The dashed line in blue color represents the rigid body moment of inertia for spherical ^{215}Fr.

the shape of the yrast lines is almost identical for both the nuclei and yields almost the same MOI. This is attributed to the fact that one pair of the $h^2_{9/2}$ protons is never broken to contribute in the yrast spectrum of ^{216}Ra [62]. An abrupt increase in the moment of inertia is observed at $I \approx 14\hbar$ in both nuclei, which suggests structural changes above this value. Further, the inset in the Fig. 12 illustrates the yrast line in ^{212}Rn ($N = 126$). The slope changes at $I \approx 19\hbar$, which corresponds to the coupling of the 5^- neutron core excitation ($g_{9/2}p^{-1}_{1/2}$) to the valence protons. A similar trend was reported in other $N = 126$ isotones, viz., ^{209}Bi, ^{210}Po, ^{211}At [62], where the classical MOI approaches the rigid body value above the spin where the core excitations start contributing to the wave function of the states. Hence, a change in the slope suggests the breaking of the ^{208}Pb core [62]. Further, it was reported that the yrast line in the doubly magic ^{208}Pb follows a linear pattern [63]. In this case, angular momentum of all the excited states is generated by the core excitations. Therefore, a change in the slope of the yrast line is not observed. However, the measured MOI was more than two times smaller compared to that of the rigid body value. This feature was explained by assuming that the nucleus (^{208}Pb) has a partial rotational contribution with an inert ^{132}Sn spherical core that does not participate in the rotation [63].

A similar structure of the yrast line is observed in ^{215}Fr as shown in Fig. 13. It is apparent that the slope of the plot changes at places along the spin scale. Therefore, the distribution of the points illustrating the yrast line may be divided into three spin ranges for further discussion: (i) $I \leqslant 25/2$, (ii) $27/2 \leqslant I \leqslant 39/2$, and (iii) $I \geqslant 41/2$. The MOI values extracted from the slope of a straight line fit are displayed in Fig. 13. The value of MOI, $2\mathcal{J}_{\text{eff}}/\hbar^2 = 102$ MeV^{-1}, in the first region is more than two times smaller compared to that of the rigid body value ($\approx$215 MeV^{-1}) for the spherical ^{215}Fr nucleus. The analogous behavior is observed in deformed nuclei, where pairing is responsible for the reduction in the MOI [52]. As more pairs break to attain higher angular momentum states, the effective MOI approaches the rigid body value. The observed features of the MOI plot in ^{215}Fr may be understood in terms of the intrinsic single-particle configurations of the states as predicted by the shell-model calculations. The angular momentum of the states lying in the first spin range is attributed to the weak coupling of the single $h_{9/2}$ or $i_{13/2}$ proton to the spin generated due to the alignment of the $g^2_{9/2}$ neutrons. The second spin region has several isomeric states, and both proton and neutron excitations contribute significantly to the wave function of the states in this region. Therefore, the transition from the dominant neutron configuration to the mixed neutron-proton configuration seems to be responsible for the change in the slope at $I \approx 25/2\hbar$. Further, the states in the $\Delta I = 2$ sequence above the $41/2^+$ level are also fitted separately. The slope of the plot results in a MOI greater than the rigid body value, which is difficult to explain using the description employed above.

V. SUMMARY AND CONCLUSIONS

High-spin states in ^{215}Fr nucleus have been studied using γ-γ coincidence measurements following the ^{208}Pb(^{11}B, $4n$)^{215}Fr reaction. The level scheme has been extended up to 4.8 MeV and $55/2\hbar$ with the addition of 52 new γ-ray transitions. A new positive-parity sequence based on the proton $i_{13/2}$ orbital has been established. The half-lives of the earlier reported isomers are confirmed and the half-life of the $39/2^-$ isomeric state has been revised to 11.4(14) ns, for which two distinctly different values were reported in the earlier studies. Furthermore, the results obtained from the centroid-shift analysis using the γ rays associated with the $27/2^-$ and $29/2^+$ states are found to be consistent with those reported by Decman *et al.* [36]. This, in turn, does not support the isomeric nature of the $27/2^-$ state. The large-scale shell-model calculations were carried out by employing the CD-Bonn NN potential derived from the $V_{\text{low-}k}$ renormalization approach. An overall good qualitative agreement has been observed between the theory and experimental data, except for the $39/2^-$ isomeric state which is underestimated by 416 keV. This may possibly be due to the octupole coupling effects, which could not be included in the shell-model calculations. In addition, the weak coupling of the odd proton to the states in the even-even core of the ^{214}Rn and ^{216}Ra is found to qualitatively account for the observed level structure in ^{215}Fr. Finally, the structure of the yrast line is found to explain the gross features of the level scheme. Future experimental as well as theoretical studies of ^{215}Fr are expected to open new understanding of the evolving physics as one moves from spherical to octupole and finally to the well deformed region.

ACKNOWLEDGMENTS

The authors would like to acknowledge the IUAC technical staff for their assistance during the experiment.

K.Y. and Pragati would like to acknowledge the financial support from MHRD, India. A.Y.D. would like to acknowledge the financial support by SERB (DST), Grant No. CRG/2020/002169. Madhu would like to acknowledge financial support from DST, India under the INSPIRE fellowship scheme (IF 180082). P.C.S. acknowledges a research grant from the Science and Engineering Research Board (SERB) of India, CRG/2019/000556. S.K.T. acknowledges support from University Grants Commission, India, under the Faculty Recharge Programme. A.K.J. acknowledges the financial support from SERB (DST), Grant No. CRG/2020/000770. The financial support by DST, India (Grant No. IR/S2/PF-03/2003-III) for the INGA project is also acknowledged.

[1] B. A. Brown and B. Wildenthal, Annu. Rev. Nucl. Part. Sci. **38**, 29 (1988).
[2] B. A. Brown, A. Etchegoyen, W. D. M. Rae, N. S. Godwin, W. A. Richter, C. H. Zimmerman, W. E. Ormand, and J. S. Winfield, MSU-NSCL Report No. 524, 1985 (unpublished).
[3] J. Blomqvist, I. Bergström, C. J. Herrlander, C. G. Lindén, and K. Wikström, Phys. Rev. Lett. **38**, 534 (1977).
[4] B. Maheshwari, D. Choudhury, and A. K. Jain, Nucl. Phys. A **1014**, 122277 (2021).
[5] I. Ahmad and P. A. Butler, Annu. Rev. Nucl. Part. Sci. **43**, 71 (1993), and references therein.
[6] P. A. Butler and W. Nazarewicz, Rev. Mod. Phys. **68**, 349 (1996).
[7] P. A. Butler, J. Phys. G: Nucl. Part. Phys. **43**, 073002 (2016), and references therein.
[8] L. P. Gaffney *et al.*, Nature (London) **497**, 199 (2013).
[9] P. A. Butler *et al.*, Nat. Commun. **10**, 2473 (2019).
[10] R. R. Chasman, Phys. Lett. B **96**, 7 (1980).
[11] P. Bonche, P. H. Heenen, H. Flocard, and D. Vautherin, Phys. Lett. B **175**, 387 (1986).
[12] J. Dobaczewski and J. Engel, Phys. Rev. Lett. **94**, 232502 (2005), and references therein.
[13] L. M. Robledo and G. F. Bertsch, Phys. Rev. C **84**, 054302 (2011), and references therein.
[14] N. V. Zamfir and D. Kusnezov, Phys. Rev. C **63**, 054306 (2001).
[15] T. M. Shneidman, G. G. Adamian, N. V. Antonenko, R. V. Jolos, and W. Scheid, Phys. Rev. C **67**, 014313 (2003).
[16] S. C. Pancholi, *Pear-Shaped Nuclei* (World-Scientific, Singapore, 2020).
[17] G. D. Dracoulis, F. Riess, A. M. Baxter, and A. E. Stuchbery, J. Phys. G: Nucl. Part. Phys. **17**, 1795 (1991).
[18] G. D. Dracoulis, A. P. Byrne, A. E. Stuchbery, R. A. Bark, and A. R. Poletti, Nucl. Phys. A **467**, 305 (1987).
[19] J. A. Cizewski and A. E. L. Dieperink, Phys. Lett. B **164**, 236 (1985).
[20] A. R. Poletti, G. D. Dracoulis, A. P. Byrne, and A. E. Stuchbery, Nucl. Phys. A **473**, 595 (1987).
[21] A. E. Stuchbery, G. D. Dracoulis, A. P. Byrne, S. J. Poletti, and A. R. Poletti, Nucl. Phys. A **482**, 692 (1988).
[22] T. Lönnroth and C. Baktash, Phys. Scr. **28**, 459 (1983).
[23] A. P. Byrne, G. J. Lane, G. D. Dracoulis, B. Fabricius, T. Kibédi, A. E. Stuchbery, A. M. Baxter, and K. J. Schiffer, Nucl. Phys. A **567**, 445 (1994).
[24] A. P. Byrne, G. D. Dracoulis, G. J. Lane, B. Fabricius, T. Kibédi, A. E. Stuchbery, A. M. Baxter, and K. Schiffer, Nucl. Phys. A **553**, 519c (1993).
[25] A. E. Stuchbery, G. D. Dracoulis, T. Kibedi, A. P. Byrne, B. Fabricius, A. R. Poletti, G. J. Lane, and A. M. Baxter, Nucl. Phys. A **641**, 401 (1998).
[26] G. D. Dracoulis, F. Riess, A. E. Stuchbery, R. A. Bark, S. L. Gupta, A. M. Baxter, and M. Kruse, Nucl. Phys. A **493**, 145 (1989).
[27] T. Lönnroth, D. Horn, C. Baktash, C. J. Lister, and G. R. Young, Phys. Rev. C **27**, 180 (1983).
[28] S. Muralithar, G. Rodrigues, R. P. Singh, R. K. Bhowmik, P. Mukherjee, B. Sethi, and I. Mukherjee, Pramana - J. Phys. **79**, 403 (2012).
[29] G. J. Lane, A. P. Byrne, and G. D. Dracoulis, in *Frontiers of Nuclear Structure, 29 July–2 August 2002, Berkeley*, edited by P. Fallon, R. Clark, and A. M. Smith, AIP Conf. Proc. No. 656 (AIP, New York, 2003), p. 386.
[30] I. Bergström and B. Fant, Phys. Scr. **31**, 26 (1985).
[31] G. D. Dracoulis, P. M. Walker, and F. G. Kondev, Rep. Prog. Phys. **79**, 076301 (2016).
[32] A. P. Byrne, G. D. Dracoulis, C. Fahlander, H. Hübel, A. R. Poletti, A. E. Stuchbery, J. Gerl, R. F. Davie, and S. J. Poletti, Nucl. Phys. A **448**, 137 (1986).
[33] M. E. Debray, A. J. Kreiner, J. M. Kesque, M. Ozafran, A. Romo, H. Somacal, M. E. Vazquez, J. Davidson, M. Davidson, K. Ahn, D. B. Fossan, Y. Liang, R. Ma, E. S. Paul, W. F. Piel, Jr., and N. Xu, Phys. Rev. C **48**, 2246 (1993).
[34] Pragati, A. Y. Deo, S. K. Tandel, S. S. Bhattacharjee, S. Chakraborty, S. Rai, S. G. Wahid, S. Kumar, S. Muralithar, R. P. Singh, I. Bala, R. Garg, and A. K. Jain, Phys. Rev. C **97**, 044309 (2018).
[35] M. E. Debray, A. J. Kreiner, M. Davidson, J. Davidson, D. Hojman, D. Santos, V. R. Vanin, N. Schulz, M. Aïche, A. Chevallier, J. Chevallier, and J. C. Sens, Nucl. Phys. A **568**, 141 (1994).
[36] D. J. Decman, H. Grawe, H. Kluge, K. H. Maier, A. Maj, M. Menningen, N. Ray, and W. Wiegner, Nucl. Phys. A **419**, 163 (1984).
[37] N. Schulz, S. Khazrouni, A. Chevallier, J. Chevallier, L. Kraus, I. Linck, D. C. Radford, J. Dudek, and W. Nazarewicz, J. Phys. G: Nucl. Phys. **10**, 1201 (1984).
[38] M. W. Drigert, J. A. Cizewski, and M. S. Rosenthal, Phys. Rev. C **32**, 136 (1985).
[39] S. Muralithar *et al.*, J. Phys. Conf. Ser. **312**, 052015 (2011).
[40] B. P. Ajith Kumar, E. T. Subramaniam, K. Rani, and K. Singh, DAE Proc. **44 B**, 390 (2001).
[41] R. Brun and F. Rademakers, Nucl. Instrum. Methods Phys. Res., Sect. A **389**, 81 (1997).
[42] D. C. Radford, Nucl. Instrum. Methods Phys. Res., Sect. A **361**, 297 (1995).
[43] J.-M. Régis, G. Pascovici, J. Jolie, and M. Rudigier, Nucl. Instrum. Methods Phys. Res., Sect. A **622**, 83 (2010).
[44] A. Krämer-Flecken, T. Morek, R. M. Lieder, W. Gast, G. Heb- binghaus, H. M. Jäger, and W. Urban,

Nucl. Instrum. Methods Phys. Res., Sect. A **275**, 333 (1989).

[45] G. Duchêne, F. A. Beck, P. J. Twin, G. de France, D. Curien, L. Han, C. W. Beausang, M. A. Bentley, P. J. Nolan, and J. Simpson, Nucl. Instrum. Methods Phys. Res., Sect. A **432**, 90 (1999).

[46] K. Starosta, T. Morek, Ch. Droste, S. G. Rohoziński, J. Srebrny, A. Wierzchucka, M. Bergström, B. Herskind, E. Melby, T. Czosnyka, and P. J. Napiorkowski, Nucl. Instrum. Methods Phys. Res., Sect. A **423**, 16 (1999).

[47] O. Klein and Y. Nishina, Z. Phys. **52**, 853 (1929).

[48] R. Palit, H. C. Jain, P. K. Joshi, S. Nagaraj, B. V. T. Rao, S. N. Chintalapudi, and S. S. Ghugre, Pramana **54**, 347 (2000).

[49] T. Yamazaki, Nucl. Data, Sec. A **3**, 1 (1967).

[50] E. der Mateosian and A. W. Sunyar, At. Data Nucl. Data Tables **13**, 391 (1974).

[51] A. Astier, P. Petkov, M.-G. Porquet, D. S. Delion, and P. Schuck, Eur. Phys. J. A **46**, 165 (2010).

[52] A. Bohr and B. R. Mottelson, *Nuclear Structure* (Benjamin, London, 1975), Vol. II.

[53] L. Coraggio, A. Covello, A. Gargano, and N. Itaco, Phys. Rev. C **80**, 021305(R) (2009).

[54] N. Shimizu, T. Mizusaki, Y. Utsuno, and Y. Tsunoda, Comput. Phys. Commun. **244**, 372 (2019).

[55] A. Goldkuhle, A. Blazhev, C. Fransen, A. Dewald, M. Beckers, B. Birkenbach, T. Braunroth, E. Clement, J. Dudouet, J. Eberth, H. Hess, B. Jacquot, J. Jolie, Y. H. Kim, A. Lemasson, S. M. Lenzi, H. J. Li, J. Litzinger, C. Michelagnoli, C. Muller-Gatermann, B. S. NaraSingh, R. M. Perez-Vidal, D. Ralet, P. Reiter, A. Vogt, N. Warr, and K. O. Zell, Phys. Rev. C **102**, 054334 (2020).

[56] J. Suhonen, *Theoretical and Mathematical Physics : From Nucleons to Nucleus* (Springer, Berlin, 2006).

[57] A. K. Jain, S. Singh, B. Singh, N. Kaur, S. Lakshami, and B. Maheshwari, Nucl. Data Sheets **114**, 1187 (2013).

[58] D. J. Decman, H. Grawe, H. Kluge, K. H. Maier, A. Maj, N. Roy, Y. K. Agarwal, K. P. Blume, M. Guttormsen, H. Hübel, and J. Recht, Nucl. Phys. A **436**, 311 (1985).

[59] S. Zhu and E. A. McCutchan, Nucl. Data Sheets **175**, 1 (2021).

[60] G. D. Dracoulis, G. J. Lane, A. P. Byrne, P. M. Davidson, T. Kibédi, P. H. Nieminen, H. Watanabe, A. N. Wilson, H. L. Liu, and F. R. Xu, Phys. Rev. C **80**, 054320 (2009).

[61] F. S. Stephens and R. S. Simon, Nucl. Phys. A **183**, 257 (1972).

[62] D. Horn, O. Häusser, B. Haas, T. K. Alexander, T. Faestermann, H. R. Andrews, and D. Ward, Nucl. Phys. A **317**, 520 (1979).

[63] R. Broda, R. V. F. Janssens, Ł. W. Iskra, J. Wrzesinski, B. Fornal, M. P. Carpenter, C. J. Chiara, N. Cieplicka-Oryńczak, C. R. Hoffman, F. G. Kondev, W. Królas, T. Lauritsen, Zs. Podolyak, D. Seweryniak, C. M. Shand, B. Szpak, W. B. Walters, S. Zhu, and B. A. Brown, Phys. Rev. C **95**, 064308 (2017).